Structure of the Western Jaz Murian Forearc Basin, Southeast Iran, Revealed by Autocorrelation and Polarization Analysis of Teleseismic P and S Waves

Haiqiang Lan, Ling Chen, Sebastien Chevrot, Morteza Talebian, Xu Wang, Yifan Gao, Jianyong Zhang, Zimu Wu, Mehdi Shokati, Mingming Jiang, et al.

JGR Solid Earth

RESEARCH ARTICLE
10.1029/2021JB023456

Structure of the Western Jaz Murian Forearc Basin, Southeast Iran, Revealed by Autocorrelation and Polarization Analysis of Teleseismic P and S Waves

Haiqiang Lan[1,2], Ling Chen[1,2,3], Sebastien Chevrot[4], Morteza Talebian[5], Xu Wang[1,2], Yifan Gao[1,2], Jianyong Zhang[6], Zimu Wu[1,2], Mehdi Shokati[7], Mingming Jiang[8,9], Yinshuang Ai[2,8,9], Guangbing Hou[8], Mulin Mao[8], Thanh-Son Phạm[10], Wenjiao Xiao[1,11], and Rixiang Zhu[1,11]

[1]State Key Laboratory of Lithospheric Evolution, Institute of Geology and Geophysics, Chinese Academy of Sciences, Beijing, China, [2]College of Earth and Planetary Sciences, University of Chinese Academy of Sciences, Beijing, China, [3]CAS Center for Excellence in Deep Earth Sciences, Guangzhou, China, [4]Observatoire Midi Pyrénées, Université Paul Sabatier, CNRS, IRD, Toulouse, France, [5]Research Institute for Earth Sciences, Geological Survey of Iran, Tehran, Iran, [6]China Earthquake Networks Center, Beijing, China, [7]Geological Survey of Iran, Tehran, Iran, [8]Key Laboratory of Earth and Planetary Physics, Institute of Geology and Geophysics, Chinese Academy of Sciences, Beijing, China, [9]CAS Center for Excellence in Tibetan Plateau Earth Sciences, Beijing, China, [10]Research School of Earth Sciences, Australian National University, Canberra, ACT, Australia, [11]Institutions of Earth Sciences, Chinese Academy of Sciences, Beijing, China

Key Points:

- We extract energetic P- and S-wave reflections from the coda of teleseismic P and S waves
- We combine these reflections with measurements of P wave polarization to resolve the structure of the western Jaz Murian sedimentary basin
- The nature of the sediments inside the Jaz Murian Basin and of the basement provides insight into the recent tectonic regime in that region

Supporting Information:

Supporting Information may be found in the online version of this article.

Correspondence to:

H. Lan,
lanhq@mail.iggcas.ac.cn

Citation:

Lan, H., Chen, L., Chevrot, S., Talebian, M., Wang, X., Gao, Y., et al. (2022). Structure of the western Jaz Murian forearc basin, southeast Iran, revealed by autocorrelation and polarization analysis of teleseismic P and S waves. *Journal of Geophysical Research: Solid Earth*, *127*, e2021JB023456. https://doi.org/10.1029/2021JB023456

Received 19 OCT 2021
Accepted 17 MAR 2022

Abstract The Jaz Murian Basin in Southeast Iran is a forearc basin that sits on top of the western Makran subduction zone. A recent seismic deployment inside the western Jaz Murian Basin documents extremely strong reverberations between the free surface and the top of the basement. These strong multiples, which hamper studies of deeper structures, carry precious information on the structure of the basin. Here we combine three independent measurements, including teleseismic P/S-wave coda autocorrelations, P-wave polarization analysis and receiver functions, to image the architecture of the western Jaz Murian Basin. The S-wave velocity structure beneath each station is constrained by teleseismic P-wave polarization analysis and a simple grid search method. In addition, both P- and S-wave reflections are extracted to measure the Poisson's ratio and the thickness of sediments, in addition to P- and/or S-wave velocities. We find that the sedimentary cover has an average thickness of ∼3 km with very low S-wave velocities around 1.2 km/s. The estimated Vp/Vs ratios are relatively high between 2.23 and 2.52, suggesting that the western Jaz Murian Basin contains unconsolidated recently deposited sediments.

Plain Language Summary Passive imaging studies usually suffer from a limited spatial resolution owing to lower frequency content and sparser acquisition compared to active source seismic experiments. On the other hand, the former are easier to perform for a fraction of the cost of the latter. In this study, we exploit teleseismic body waves recorded by our recently deployed temporary array in the western Jaz Murian forearc basin, southeast Iran. Our results reveal the detailed structure of the western Jaz Murian sedimentary basin, mostly filled with unconsolidated sediments, possibly originating from lake deposition.

1. Introduction

The Jaz Murian Basin is a forearc basin that sits on top of the Makran subduction zone, where the Arabian plate currently subducts beneath the Eurasian plate, developing one of the largest accretionary wedges on Earth (e.g., Burg, 2018; Esmaeili et al., 2020; Priestley et al., 2022; Stern et al., 2021). The basin is located between the magmatic arc (with the Bazman and Taftan volcanoes) to the north and the accretionary prism to the south in southeastern Iran (e.g., Smith et al., 2012; Figures 1a and 1b). It has recorded the evolution of the arc-trench system (Ingersoll, 1988; Wang et al., 2017), which is crucial to unravel the dynamics of the subduction initiation, and/or the role of extension in the upper plate (Hopson et al., 2008). Until now, only a few geophysical studies have been performed in that region, with insufficient spatial resolution to constrain the basin architecture (e.g., Amini et al., 2012; Simmons et al., 2011); recent magnetic studies documented large positive anomalies within or beneath the Jaz Murian Basin (Abedi & Bahroudi, 2016; Teknik & Ghods, 2017). Onshore deep seismic sounding profiles which extended to the southern margin of the Jaz Murian Basin showed that the sedimentary basin thickens gradually from the western margin to the center of the basin (Haberland et al., 2021). Its structural

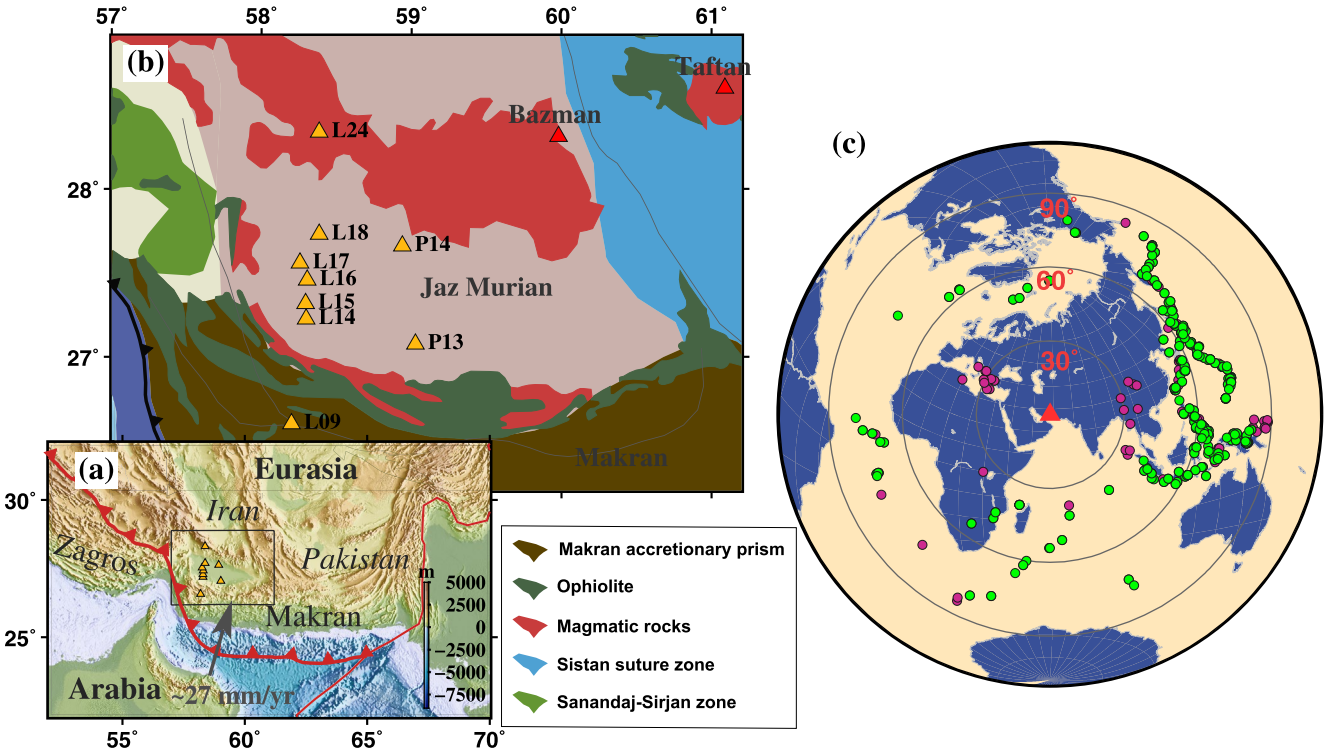

Figure 1. (a) Topographic map of the Jaz Murian and adjacent areas. The black box delimits the area shown in (b). Plate boundaries are marked by red lines. The gray arrow shows the GPS velocity of Arabia relative to Eurasia (Vernant et al., 2004). Jaz M: Jaz Murian Basin. (b) Seismic stations (orange triangles) and major tectonic boundaries in the study region. Geological basemap is modified from the structural map of NGDIR (National Geoscience Database of Iran, http://www.ngdir.ir). (c) Distribution of the teleseismic P- and S-wave events used, marked by magenta and green dots, respectively. Epicentral distances from the center of the study region (red triangle) are noted on concentric circles.

complexity is further revealed by a receiver function study transect across the eastern edge of the basin (Priestley et al., 2022).

A passive seismic transect was deployed in 2017–2018 across the western Makran accretionary wedge, with 5 stations located inside the Jaz Murian Basin (Figure 1b). The receiver functions at these 5 stations show unusually strong near-surface reverberations, which are not observed on the adjacent stations located outside of the basin. Indeed, the contamination of teleseismic body wave records is so strong that it prevents detailed imaging of the deeper structures. Therefore, the main motivation of this study is to investigate these unusual P and S reverberations and constrain the detailed structure of the Jaz Murian Basin.

To date, the most effective (but by far also the most expensive) method to constrain the structure of shallow crust in general and sedimentary basins in particular is to drill boreholes and measure rock properties in the laboratory (e.g., Greenberg & Castagna, 1992; Tang et al., 2004). Active source methods have also been widely used for oil and gas exploration as well as deep seismic sounding (e.g., Mooney et al., 1998; Yilmaz, 2001; Zhang et al., 2011). Generally, active source acquisitions offer a finer resolution due to their higher frequency content, but they are expensive and hardly constrain S-wave velocities (Wittlinger & Farra, 2015). By contrast, passive imaging methods which exploit natural earthquakes can also image the subsurface (e.g., Ritzwoller et al., 2002; Zhu, 2000). However, traditional passive imaging methods utilizing teleseismic data, for example, tomographic methods based on body waves (e.g., Lei & Zhao, 2009; Liang et al., 2004) or surface waves (e.g., Friederich, 1998; Jiang et al., 2013) or receiver function methods which are helpful to image subsurface discontinuities (e.g., Chen et al., 2005; Ligorria & Ammon, 1999), have limits or deficiencies in constraining kilometer-scale shallow structures owing to both lower frequency contents and sparser acquisitions (Badal et al., 2013), and thereby mostly are used in imaging larger-scale structures, such as the whole crust and/or a large part of the mantle, although large-scale acquisitions are experiencing rapid development (e.g., Lin et al., 2013; Nakata et al., 2015; Tian et al., 2021).

Table 1
Number of Seismograms Used in the Computation of the Autocorrelation Stacks for All Station Components After the Visual Qualification Control

	P-wave autocorrelations			S-wave autocorrelations		
Station	Vertical	Radial	Transverse	Vertical	Radial	Transverse
L14	226	151	88	69	125	107
L15	165	119	80	63	89	70
L16	179	128	93	41	107	86
L17	192	101	90	71	88	88
L18	145	71	48	59	90	68
P13	196	191	190	56	131	137
P14	195	171	-	55	149	-

Note. "-" indicates no valid reflected waves extracted from this component.

From the autocorrelations of teleseismic body-wave (P and S wave) codas it is possible to extract reflected phases to image subsurface sharp discontinuities (Ruigrok & Wapenaar, 2012; Sun & Kennett, 2016). For example, Phạm and Tkalčić (2018) successfully applied this method to measure the thickness of the ice sheet in Antarctica, with results in good agreement with the Bedmap2 model of ice thickness compiled mostly from airborne radio-echo sounding measurements (Fretwell et al., 2013). The very strong amplitudes of reverberations in the western Jaz Murian Basin motivated us to apply this coda autocorrelation method for which very few successful attempts have been reported so far applied to study sedimentary basins (e.g., Chimoto & Yamanaka, 2020; Plescia et al., 2021). The P-wave polarization method is an interesting complementary method to infer near-surface S-wave velocity structures in addition to the interface structure (e.g., Chong et al., 2018; Hannemann et al., 2016; Svenningsen & Jacobsen, 2007; Wang et al., 2019).

In this study, we perform a comprehensive study of the western Jaz Murian Basin structure by combining different passive approaches such as teleseismic P and S coda wave autocorrelation and teleseismic P wave polarization analysis. The paper is organized as follows. We first describe the data and method used in this study, including some processing details considering the particularity of the Jaz Murian data. We then synthesize new information that has been collected regarding the basin structure, discuss its implications for the recent evolution of the Jaz Murian sedimentary basin, and finally give some perspectives for future studies.

2. Data and Methods

2.1. Data

The seismic data used in this study were recorded by 5 broadband temporary stations (L14, L15, L16, L17 and L18) located in the western Jaz Murian Basin, from the main transect of a China-Iran geological and geophysical survey in the Iranian plateau (CIGSIP; Figures 1a and 1b). The seismic stations were deployed along a roughly N-S line, from the southern end of the magmatic arc to the northern border of the ophiolitic complex, with a spacing of ∼10–15 km. In addition, we also analyzed data from four other stations for comparison. Of these, two were also from the main line, in the southern Makran accretionary wedge (L09) and the northern magmatic arc (L24), respectively. Another two stations were from an eastern offline about 70 km from the main line, lying near the south- (P13) and north-margin (P14) of the central Jaz Murian Basin respectively. All stations were equipped with Trillium 120PA seismometers (120 s - 175 Hz) and Taurus digital seismographs, and operated from March 2017 to September 2018.

We retrieve three-component teleseismic records of events in the USGS National Earthquake Information Center catalog with Mw $\geq$ 5.0 and in the epicentral distance ranges of respectively 28°–92° for P waves, and 50°–90° for S waves. The selected events are shown in Figure 1c. We select seismograms with high signal-to-noise ratios (SNRs) around the P- and S-wave onsets. We consider 40 s time windows starting 10 s before the theoretical P/S arrival time predicted by the reference model AK135 (Kennett et al., 1995). Table 1 shows the number of selected traces for each component at each station. For P-wave coda, the SNR on vertical (Z) component is typically higher than that on the horizontal components. Conversely, for the S-wave coda, the SNRs on the horizontal components are higher than their vertical counterpart.

2.2. Extracting P- and S-wave Reflections From Autocorrelations

The transmission response of a medium can be transformed into its reflection response through autocorrelation (Claerbout, 1968; Frasier, 1970; Wapenaar et al., 2004). This approach has been applied to records of ambient seismic noise to extract body-wave reverberations and image crustal and upper mantle reflectors (Badal et al., 2013; Gorbatov et al., 2013; Kennett, 2015; Sun et al., 2018; Taylor et al., 2016; Tibuleac & von Seggern, 2012). Recent studies have shown that the autocorrelation approach can also be applied successfully to the coda of teleseismic P waves (Phạm & Tkalčić 2017, 2018). Compared to studies relying on ambient seismic noise, which always require a large amount of data (months to years), this latter approach requires a much smaller amount of

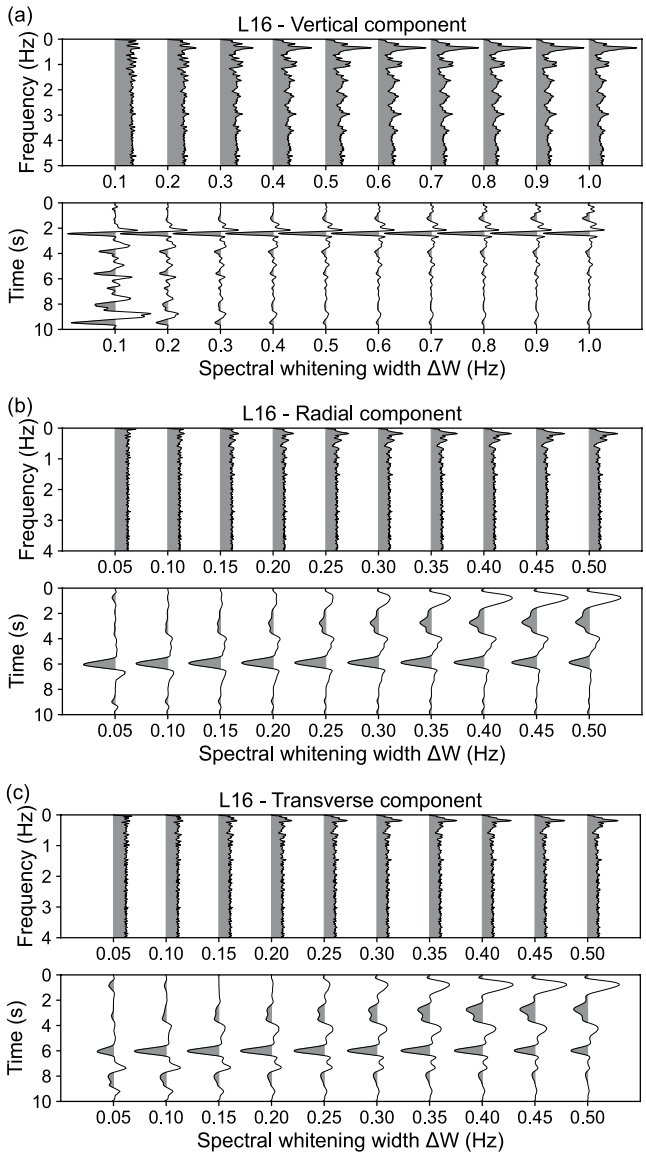

Figure 2. Effects of spectral whitening width ΔW on autocorrelations, computed for the vertical component of the teleseismic P-wave coda recorded by station L16 (a); radial (b) and transverse (c) components of the teleseismic S-wave coda, respectively. The upper panel in each sub-plot is the linear stacks of power spectra, whereas the lower panel is the corresponding temporal autocorrelations for different whitening widths. The central peaks at 0 s onset are tapered by a cosine function.

quality-controlled data and computational efforts to produce a comparable reflectivity record (Fang & Hilst, 2019; Lin & Tsai, 2013). Note that, Phạm and Tkalčić (2018) used vertical and radial components of P-wave coda records to extract the P- and S-wave reflections respectively. In this study, we consider vertical autocorrelations of teleseismic P-wave coda and horizontal autocorrelations of S-wave coda as there are usually higher signal-to-noise ratios on the corresponding components.

To improve the detection of reflected phases, we follow the recipe presented in Phạm and Tkalčić (2017). We first transform the selected waveforms to the spectral domain and normalize them by spectral whitening over a frequency bandwidth ΔW. This normalization is crucial to enhance the resonance peaks related to the sedimentary layer. The optimal width for the spectral whitening ΔW needs to be chosen as between one and two resonance peak spacings, which is the reciprocal of the vertical two-way travel time in the layer, as shown in Phạm and Tkalčić (2018). Since at this point the vertical two-way travel time is not known, the optimal ΔW needs to be tuned by trial and error.

We select vertical component teleseismic P waves recorded by station L16 to illustrate the tuning of the spectral whitening bandwidth (Figure 2a). We first compute the power of the whitened spectrum, which cancels the phase spectrum and only retains the square of the amplitude spectrum. The power spectrum is then transformed back into the time domain. Hereafter, we isolate the causal (positive offset) one-sided autocorrelograms, and apply a cosine taper to suppress the 0-delay central pulse. Finally, the autocorrelograms are filtered with a zero-phase high-pass filter to enhance the reflected arrivals. We calculate autocorrelations (lower panel in Figure 2a) and their corresponding power spectra (upper panel in Figure 2a) inside 10 spectral bandwidths from 0.1 to 1.0 Hz with intervals of 0.1 Hz. When the whitening widths are larger than 0.4 Hz, resonance peaks corresponding to P reflections start to emerge from the power spectra. The spacing of the peaks (~0.41 Hz) is the reciprocal of the vertical two-way travel time ($\tau \approx 2.42$ s, picked from the temporal autocorrelograms).

For the radial (R) and transverse (T) autocorrelograms, we also consider 10 spectral bandwidths starting from 0.05 Hz with a step of 0.05 Hz. In the following, we only show the R and T autocorrelograms from the teleseismic S-wave coda. The corresponding power spectra and temporal autocorrelations are shown in Figures 2b and 2c, respectively. The resonance effect is also observed in the horizontal components power spectra, with regularly spaced resonance peaks up to ~1.3 Hz detected when the whitening widths are larger than 0.15 Hz. From these tests, we choose 0.4 Hz for the whitening width in the vertical component autocorrelations and 0.15 Hz for the radial and transverse component autocorrelations. The other stations were analyzed following the same procedure (see Table S1 in Supporting Information S1).

Filtering is a key ingredient for reverberation detections. According to the sampling theorem, the longest wavelength should be approximately 4 times the sediment thickness (Phạm & Tkalčić, 2017). Assuming that the thickness of the sedimentary layer beneath L16 is 3 km with S wave velocity of ~1 km/s (as revealed by the P-wave polarization later), the longest wavelength should be ~12 km, so the frequency threshold is ~0.08 Hz for the horizontal components and ~0.16 Hz for the vertical component respectively with the assumption of Vp/Vs about 2.5. However, the waveforms must contain much higher frequencies in order to resolve the base of the sedimentary basin. After extensive testing, we found that the frequency bandwidth 0.2–1.3 Hz, with wavelengths equivalent to 0.8–5 km, is suitable for the radial and transverse components of L16. As for the vertical component, the appropriate frequency band is

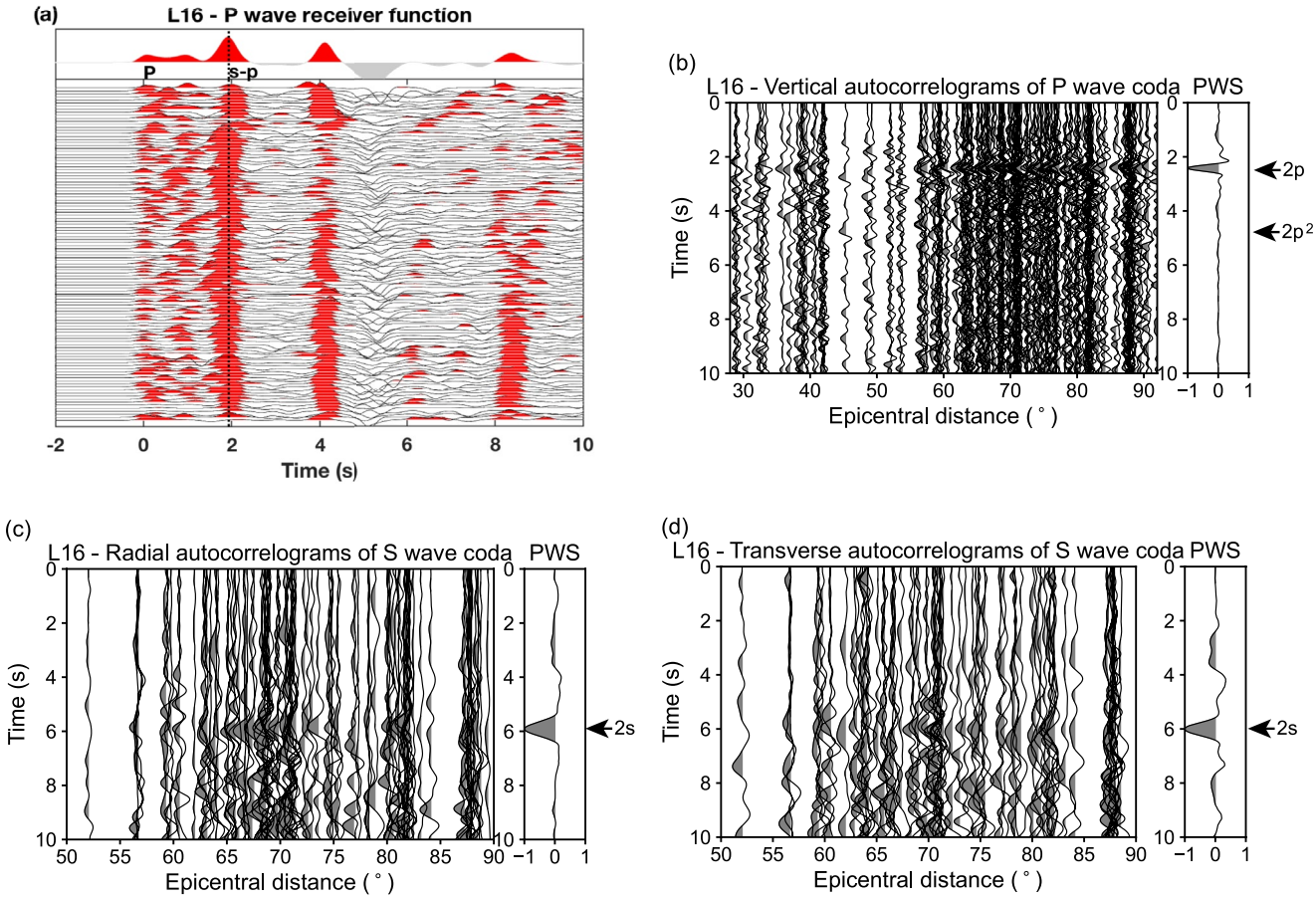

Figure 3. (a) P-wave receiver function computed by an iterative deconvolution method (Ligorria & Ammon, 1999) for station L16. "P" denotes the direct P wave which arrives first on the seismogram, "s-p" denotes the converted Ps phase at the subsurface discontinuity. (b)–(d) One-sided whitened autocorrelograms of records at station L16: (a) Vertical autocorrelograms from P-wave coda autocorrelation, "2p" denotes the P wave single reflection, "2p²" denotes the P wave twice reflections; (b) radial and (c) transverse autocorrelograms from S-wave coda autocorrelation, "2s" denotes the S wave single reflection.

0.5–3 Hz. The optimal filtering parameters for other stations were analyzed following the same procedure. The data processing parameters for the different stations are listed in Table S1 in Supporting Information S1.

We stack the autocorrelations of individual events with a phase-weighted stacking (PWS) method (Schimmel & Paulssen, 1997) to improve the signal-to-noise ratio and suppress incoherent features such as the effects of source time functions, depth phases, and source-side scattering (Phạm & Tkalčić, 2017). The autocorrelograms obtained for the stations in the Jaz Murian are shown in Figures 3–7(b-d), respectively. Here, we only show the *Z* autocorrelograms derived from the teleseismic P-waves and the *R* and *T* autocorrelograms derived from the teleseismic S waves. Results for other components are supplied in Figures S1–S5 in Supporting Information S1.

We use a bootstrap resampling method (Efron & Tibshirani, 1991) to determine the reflection delays and their uncertainties. Here, we mainly consider the uncertainty of the observation itself, as the observational data themselves have a degree of dispersion. The mean and standard deviation of 1,000 sets of resampling tests represent the estimates for the two-way reflection time t_{2x} and its associated error δt_{2x}. When the estimated error bounds are smaller than the sampling interval $\Delta t = 0.02$ s, we use the sampling step as the error bound, that is, $\delta t_{2x} = \Delta t$. Overall, the P- and S-wave reflection two-way travel times are summarized in Table 2. Using the two-way P-wave reflection time t_{2P} measured on the vertical P-wave autocorrelations, and $\Delta t^{RF}_{S-P} = t_S - t_P$ (Table 2), the differential travel times between the P-to-S conversion and the direct P wave measured from receiver functions (RF; Figures 3–7a), we can also obtain the S-wave reflection time indirectly through the relation $t_{2S} = 2\Delta t^{RF}_{S-P} + t_{2P}$. These S-wave reflection travel times are in good agreement with those directly picked on the horizontal

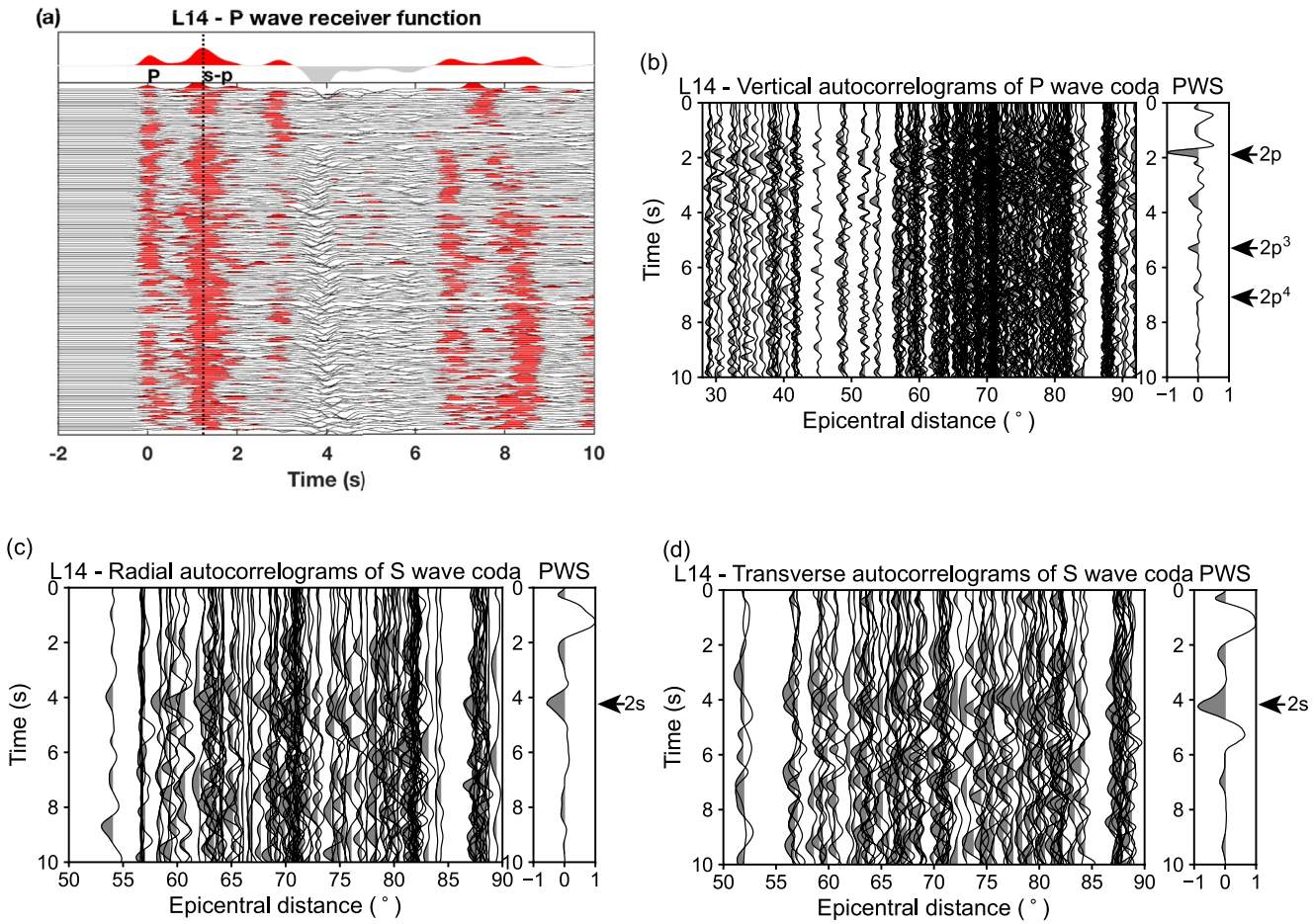

Figure 4. The same as Figure 3 but for station L14. The labels are the same meaning as that of Figure 3, except "$2p^3$" and "$2p^4$" denote the P wave three- and four-times reflections, respectively.

autocorrelograms (Table 2), which gives us confidence on the quality of the S-wave reflections detected in the autocorrelograms.

So far, we have implicitly assumed that the P and S waves have normal incidence. We now estimate the errors that could result from this simplified assumption. For a 3 km thick sedimentary layer with Vp = 2.5 km/s and Versus = 1.2 km/s, an average ray parameter p of 0.054 s/km, the maximum reflection delay time corresponding to vertical incidence is $2H/V_P$, where H represents the thickness. The delay time corresponding to a ray parameter p is $2H\sqrt{\frac{1}{V_P^2} - p^2}$, which differs by less than 1% from the vertical propagation. Similarly, the error on the two-way travel time of S wave reflections is also less than 1%. Therefore, from now on we will consider that the two-way reflection times measured in the stacks (Figures 8a and 8b) are simply the vertical two-way travel times.

2.3. Constraining S-Wave Velocities From P-Wave Polarization Analysis

When the teleseismic P wave reaches a station located on Earth's surface, the interaction of the incident wave with the free surface generates reflected and converted waves, and the particle motion is controlled by the complex interference between P and SV incident and reflected waves (see Figure S6 in Supporting Information S1). The apparent polarization of the particle motion (incidence angle φ_P) results from the superposition of the displacements produced by the incident P wave and all the reflected/converted waves. The apparent P wave incidence angle φ_P therefore differs from the theoretical incidence angle of the vertically propagating P wave. Wiechert (1907) and later Svenningsen and Jacobsen (2007) showed that, at the free surface, the apparent P wave incidence angle φ_P is twice the angle of the reflected SV wave, and that the polarization directions of teleseismic

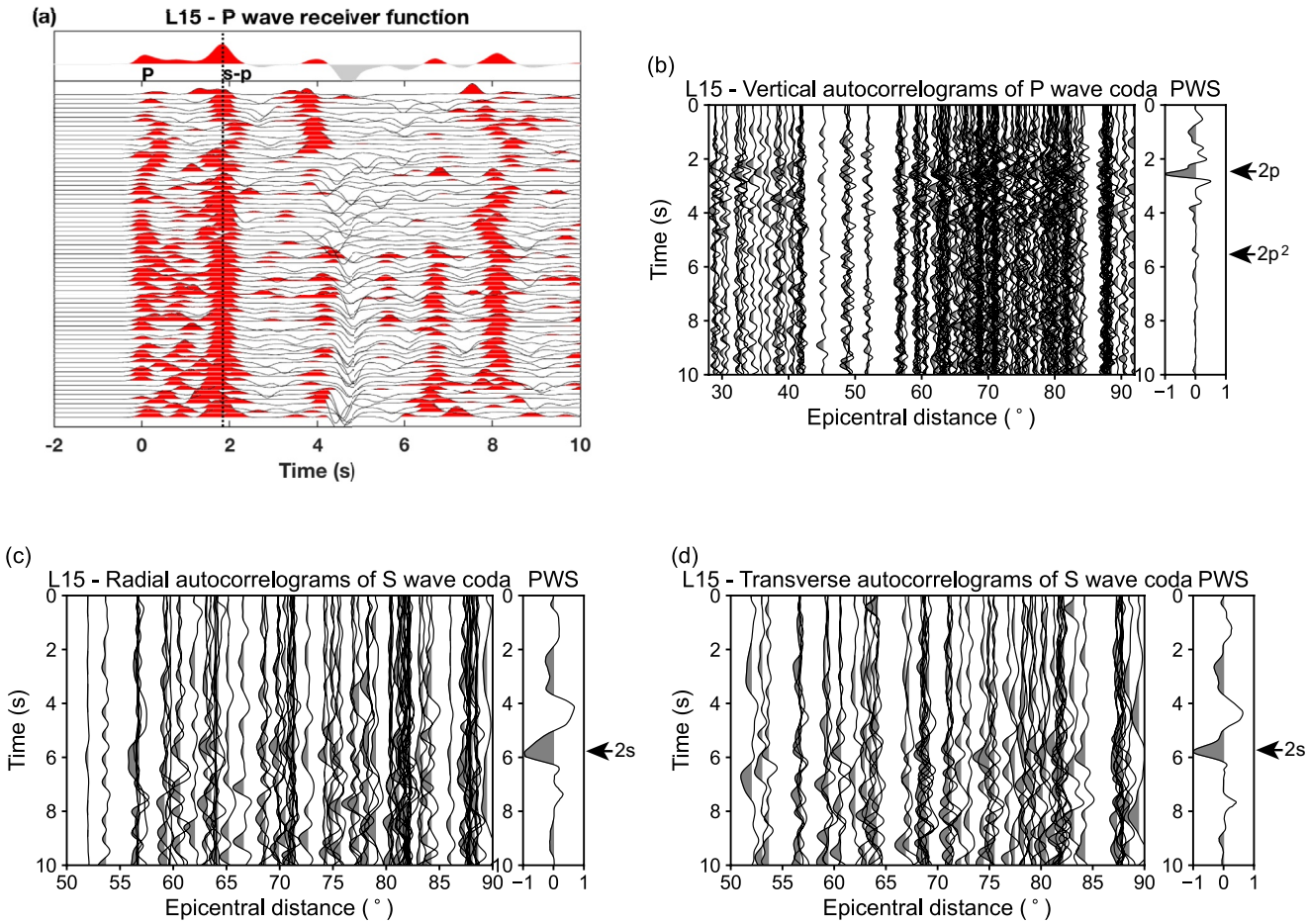

Figure 5. The same as Figure 3 but for station L15.

P waves observed at the surface are sensitive only to S wave velocity. Therefore, it is possible to infer the near surface shear wave velocity structure from the apparent polarization of teleseismic P waves, as previously noted by Wiechert (1907), Svenningsen and Jacobsen (2007), and Park and Ishii (2018).

Different time and frequency domain algorithms have been developed to measure the polarization of seismic waves from three-component records (Bataille & Chiu, 1991; Du et al., 2000; Park et al., 1987; Park & Ishii, 2018; Vidale, 1986; Wagner & Owens, 1995). Here, we use the (*Z*, *R*) receiver functions (RFs) instead of the raw (*Z*, *R*) traces to compute the apparent polarization angle φ_P in order to mitigate the influence of the P-waveform on apparent S wave velocity (VS, app.; Svenningsen & Jacobsen, 2007). The RFs (RRF, ZRF) are computed with an iterative deconvolution method (Ligorria & Ammon, 1999). We can measure the variations of φ_P with period T by filtering the RFs in different period bands (Figures 9a and 9b). We then obtain values of apparent VS as a function of observing period that can be used to infer the variations of S-wave velocity with depth (see Svenningsen & Jacobsen, 2007 for further details)

$$Vs, app.(T) = \frac{sin\left(\frac{\varphi_{P(T)}}{2}\right)}{p}. \quad (1)$$

Figures 10a–10e show our $V_{S,\,app}$. (T) measurements for the western Jaz Murian stations. To remove outliers, we only keep values within the 68% fraction closest to the median (blue curve) at each T, plotted with light gray dots. The mean value and estimates based on stacked RF (red curves) are also shown in each figure. For Gaussian errors this 68% fraction equals one standard deviation and the median equals the mean. For non-Gaussian errors the median is a more robust estimate, although the difference is minimal in most cases (Svenningsen &

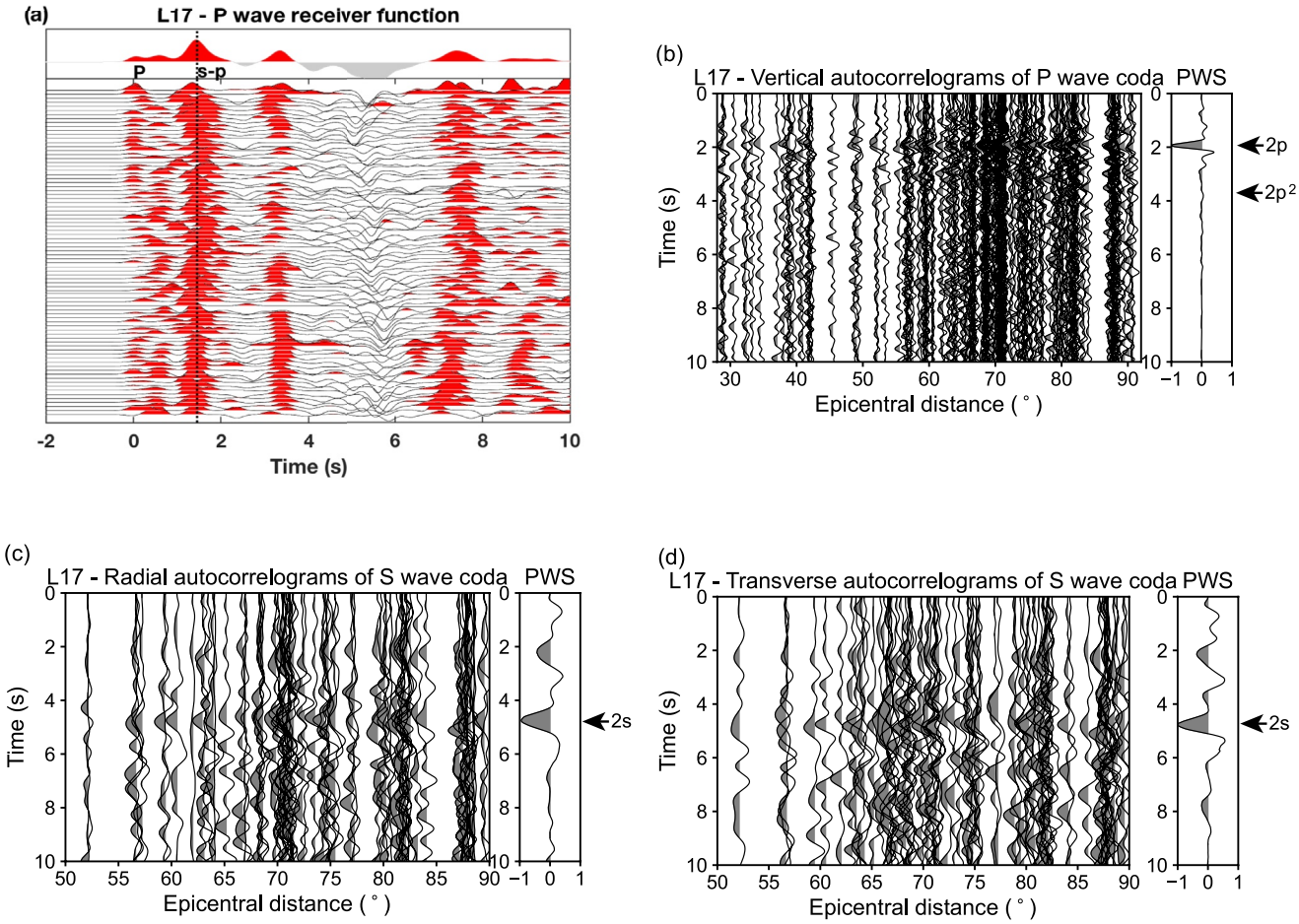

Figure 6. The same as Figure 3 but for station L17.

Jacobsen, 2007). The three estimates for stations L14, L15, and L18 are very close, while the medians of L16 and L17 are smaller than the means.

In addition, we also show the $V_{S,\,app}$. (T) curves for the two stations outside of the Jaz Murian Basin (i.e., L09 and L24; Figures 11a and 11b). We can see the apparent velocities near the surface are much smaller for the Jaz Murian stations than those from these two stations; furthermore, the apparent velocity increases at a much higher rate (with the period) for Jaz Murian stations, which implies that the velocity variation beneath Jaz Murian Basin is significantly larger than its surroundings. This is also revealed in the comparisons of receiver functions between the Jaz Murian stations (Figures 3a–7a) and those two (Figures 11c and 11d), with the Ps converted wave from the base of the basin (s-p) and the subsequent multiples clearly appearing only in the Jaz Murian stations.

We invert the S-wave velocity structure from the median $V_{S,\,app}$. (T) curve obtained for each station via a simple grid search. We illustrate the effectiveness of this method through a number of numerical experiments in the supplementary material (Figures S7–S8, Tables S2–S4 in Supporting Information S1). We represent the underground structure of the western Jaz Murian Basin with three-layer models. The top two layers represent the sedimentary basin and the bottom layer represents the basement. The grid search interval for each parameter is defined based on a careful inspection of the apparent S-wave velocity curves. We invert the apparent velocities at 5 different periods (T): 2, 3, 4, 5, and 6 s (Figure S9 in Supporting Information S1). At shorter periods, the apparent velocities carry information on structures at shallow depths, and the sensitivity shifts to deeper depth levels when the period increases. From this analysis, we determine the thickness of the sedimentary layer, the S-wave travel time and average velocity combining the results obtained for all the periods (Table S5 in Supporting Information S1). We keep the value that provides the closest S-wave travel time to that obtained from S-wave autocorrelations (Table 2). If there are multiple periods having similar travel times that are close to the autocorrelations,

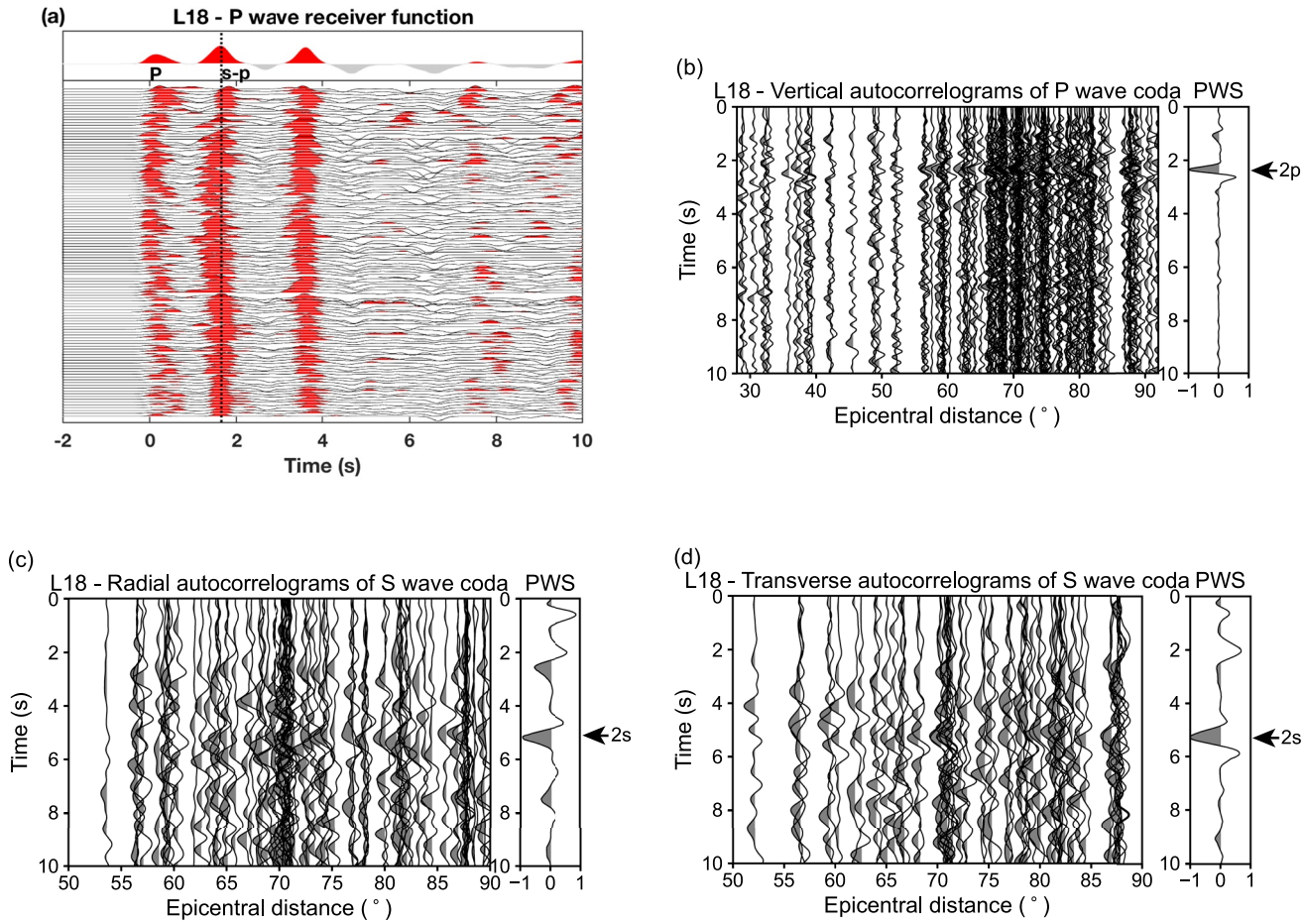

Figure 7. The same as Figure 3 but for station L18.

we favor the one in which the thickness of the sedimentary layer (directly inverted by the apparent velocity curve) is closest to that determined by the average velocity and the reflected wave travel time picked from the autocorrelograms (e.g., station L16).

3. Seismic Properties of Western Jaz Murian Basin

Our final model for the western Jaz Murian Basin is shown in Figure 12. The average shear wave velocities determined from bootstrap ananalysis beneath each station are 1.24, 1.38, 1.10, 0.98, and 1.35 km/s, respectively. The average shear wave velocities and two-way S-wave travel times can now be exploited to derive additional properties of the sedimentary layer, such as the sediment thickness (H), V_P, and V_P/Vs ratios.

Table 2
Spectral Whitening Bandwidths and Estimated P- and S-Wave Reflection Times

Station	Δw_z	$\Delta w_{r,t}$	$\Delta t^{RF}_{S-P}(s)$	t_{2P} (s)	t_{2SV} (s)	t_{2SH} (s)	$2\Delta t^{RF}_{S-P} + t_{2P}(s)$
L14	0.5	0.20	1.17	1.81 ± 0.02	4.22 ± 0.02	4.21 ± 0.03	4.15
L15	0.4	0.15	1.75	2.56 ± 0.02	5.83 ± 0.07	5.79 ± 0.02	6.06
L16	0.4	0.15	1.82	2.41 ± 0.02	5.91 ± 0.02	6.01 ± 0.02	6.05
L17	0.5	0.20	1.38	1.94 ± 0.02	4.75 ± 0.02	4.76 ± 0.02	4.70
L18	0.5	0.20	1.48	2.34 ± 0.02	5.18 ± 0.02	5.26 ± 0.04	5.30

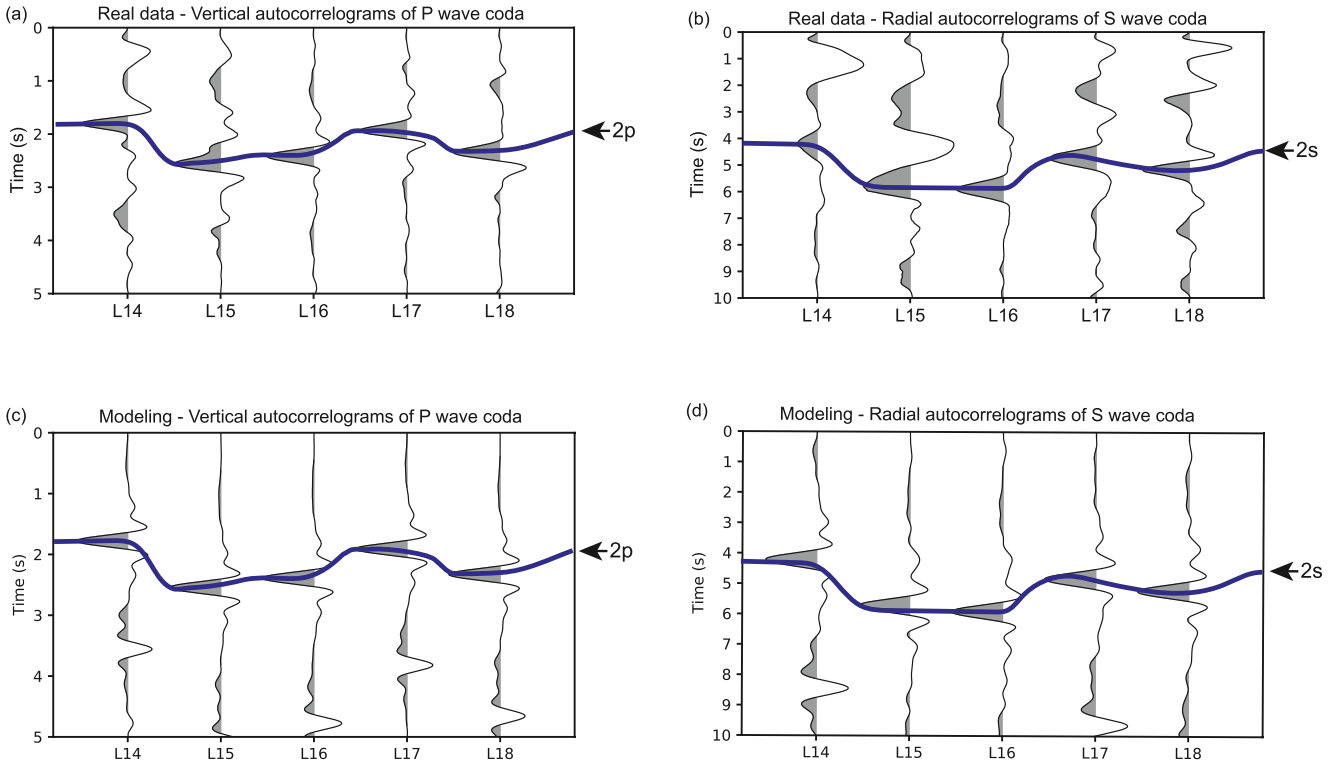

Figure 8. (a) Stacked vertical autocorrelograms from P-wave coda autocorrelation for Jaz Murian data; (b) stacked radial autocorrelograms from S-wave coda autocorrelation for Jaz Murian data; (c) stacked vertical autocorrelograms from P-wave coda autocorrelation obtained from synthetic seismograms computed in the model described in Table S6 in Supporting Information S1; (d) stacked radial autocorrelograms from S-wave coda autocorrelation obtained from synthetic seismograms computed in the model described in Table S6 in Supporting Information S1. The blue solid line connects the P-wave reflection (a), (c) and S-wave reflection (b), (d) at each station.

The sediment thickness and its uncertainty can be estimated using the travel times of S-wave reflections t_{2S} from the horizontal autocorrelograms and Versus from the P-wave polarization analysis (Phạm & Tkalčić, 2018)

$$H = \frac{t_{2S} V_S}{2}, \tag{2}$$

$$\delta H = \frac{\delta t_{2S} V_S + t_{2S} \delta V_S}{2}. \tag{3}$$

The estimated sediment thickness beneath each station is shown in Figure 13. These estimates are close to those inverted from the apparent velocity curves, which suggests that they are both accurate and robust. Considering station L16 as an example, the thickness of the sedimentary layer is about 3 km. For wavelengths between 0.8 and 5 km, this is equivalent to a sampling of 1.2–7.5 wavelengths in each reflective layer, which satisfies the requirements of the sampling theorem (at least 1 wavelength in a reflective layer).

Since the P- and S-wave reflection times are obtained separately from the stacks, we can recover the average V_P/V_S ratio (κ) of the sedimentary layer by taking the ratio of the delay times

$$\kappa = \frac{t_{2S}}{t_{2P}}. \tag{4}$$

The error bounds of the V_P/V_S ratio is propagated from the time pick error bounds as

$$\delta\kappa = \frac{\delta t_{2S}}{t_{2P}} - \frac{t_{2S}\delta t_{2P}}{{t_{2P}}^2}. \tag{5}$$

The V_P/V_S ratio can then be converted into Poisson's ratio using

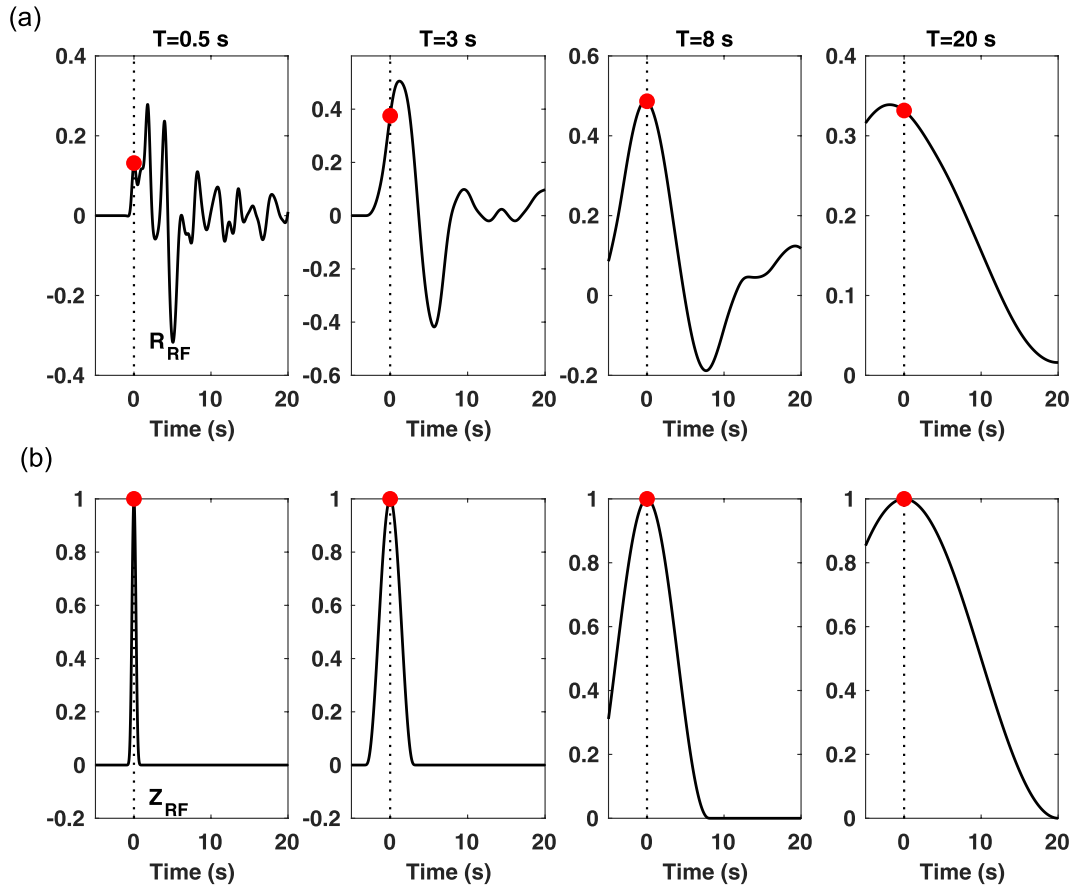

Figure 9. Low-pass filtered (smoothed) using four different filter-parameters T, for the stacked receiver functions of L16 station. (a) R_{RF} and (b) Z_{RF}. The values of T are written on each plot and the amplitudes of R_{RF} and Z_{RF} at $t = 0$ are marked with red dots.

$$\sigma = \frac{\left(\kappa^2 - 2\right)}{2\left(\kappa^2 - 1\right)}, \tag{6}$$

$$\delta\sigma = \frac{k\delta\kappa}{\left(\kappa^2 - 1\right)} - \frac{2k\left(\kappa^2 - 2\right)\delta\kappa}{2\left(\kappa^2 - 1\right)^2}, \tag{7}$$

In addition, the P-wave velocities can be obtained using the relation $V_P = V_S\,\kappa$. The structural information (thickness (H), V_P, V_S, V_P/V_S ratio (κ) and/or Poisson's ratio (σ)) beneath each station is summarized in Figure 13. The results show that in the western Jaz Murian Basin, the sediment thickness is around 3 km, the S wave velocity around 1.2 km/s and the compressional velocity around 2.9 km/s. The estimated V_P/V_S ratios are relatively high, between 2.2 and 2.5.

The presence of faults, fractures, and more generally tectonic stresses in the sedimentary layer may induce seismic anisotropy (e.g., Backus & George, 1965; Crampin & Chastin, 2003). This seismic anisotropy may bias wave velocity estimates. We examine this potential bias similarly to Park and Ishii (2018). Considering the average compressional and shear wave velocities obtained in this study, and an azimuthal anisotropy of 5–20% (e.g., Boness & Zoback, 2006; Daley & Mcevilly, 1990), we estimate a maximum bias of 0.05 km/s for P wave velocity and 0.02 km/s for S wave velocity, smaller than the average uncertainties of 0.25 km/s for P and 0.08 km/s for S wave velocity estimates. Thus, the contribution of seismic anisotropy is within the uncertainty of wave velocity estimates, even if a strong (20%) anisotropy is considered.

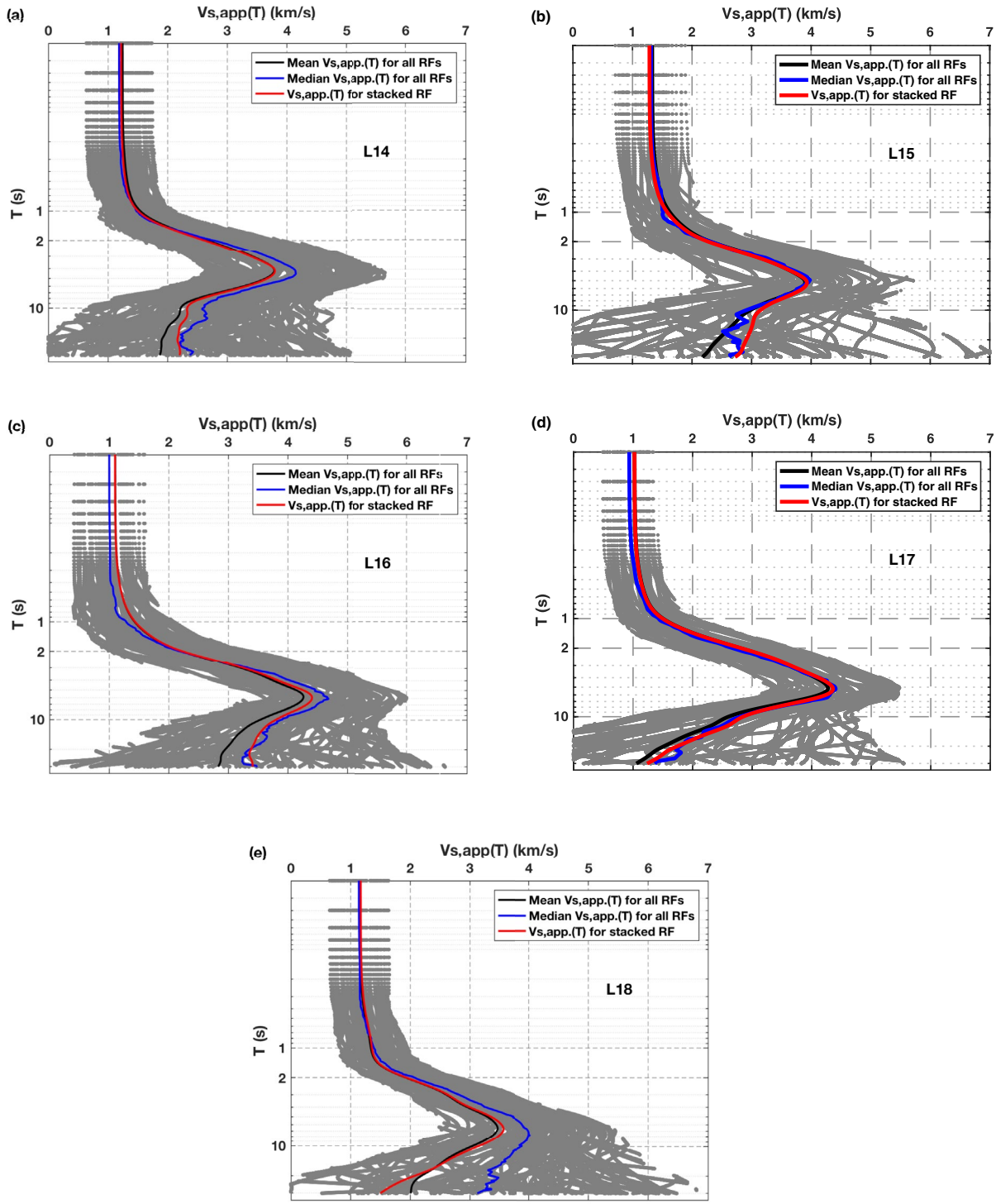

Figure 10. (a)–(e) show $V_{S,\,app}$. (T) estimates for the western Jaz Murian stations. For each T the light gray dots mark the 68 percent fraction of the estimates closest to median, shown as the blue curve. The mean estimates and those estimates made for the stacked RF are also shown in each figure, represented by black and red lines, respectively.

We also use the wavenumber integration method of Chapman (1978) from Computer Programs in Seismology (Herrmann, 2013) to compute the synthetic seismograms of teleseismic P and S waves. The method provides complete solutions in a 1-D layered model, including all of the multiples. The autocorrelograms computed on the

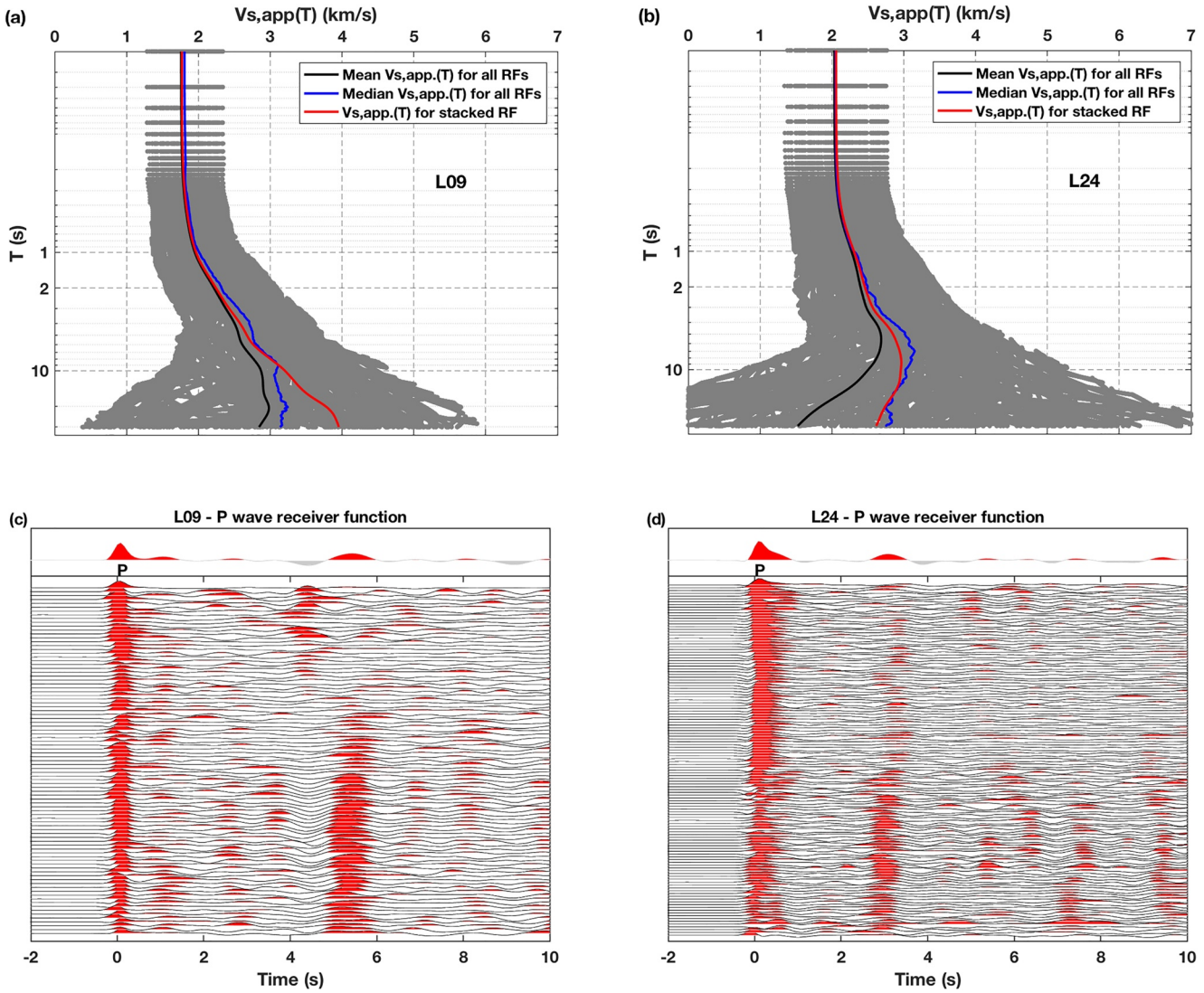

Figure 11. $V_{S,\,app}$. (T) for stations L09 (a) and L24 (b): L09 is located at the Makran accretionary wedge, whereas L24 is located at the southern margin of the Makran magma arc; (c) and (d) are P wave receiver functions for these two stations respectively.

synthetic seismograms match very well with those derived from the real data (Figures 8c and 8d), which further supports our results for the western Jaz Murian Basin.

In order to highlight the anomalous signature of seismic records in the western Jaz Murian Basin, we also analyzed two other stations to the east of the 5 main stations, that is, P13 and P14. The results of teleseismic coda autocorrelation and P-wave polarization analysis for P13 and P14 are shown in Figures S10–12 in Supporting Information S1, respectively. The measured two-way travel times are 2.07 ± 0.02 s for P-wave reflection and 4.55 ± 0.03s for S-wave reflection for P13; whereas for P14, they are 2.65 ± 0.02 s for the P-wave reflection and 6.10 ± 0.02s for the S-wave reflection. The estimated V_P/V_S ratios are between 2.19 and 2.31 for these two stations. The average shear wave velocities beneath both P13 and P14 are around 1.35 km/s, whereas the sediments are ~3.1 and ~4.1 km thick, respectively. Although we do not give a fine structure for the whole basin, the western part of the basin is accurately characterized, with the thicknesses matching well with the range of Teknik and Ghods (2017) where they overlap. On the other hand, the particular results obtained in the western Jaz Murian Basin may reveal an anomalous nature, which may provide a window for exploring its formation and the evolution of the Makran subduction zone.

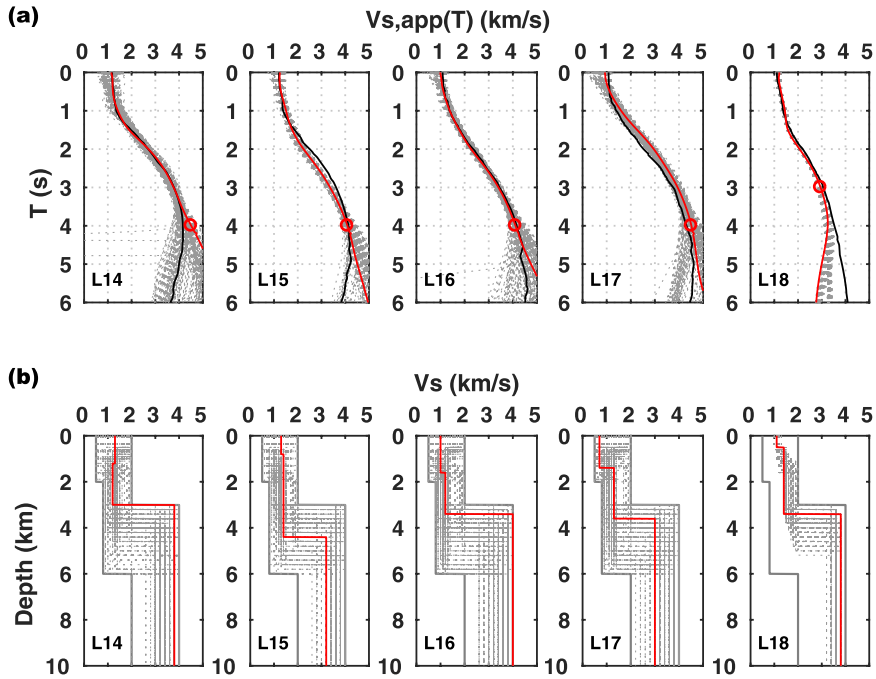

Figure 12. A simple grid search inversion of apparent velocity curves for Jaz Murian stations. (a) Synthetic apparent velocity curves for Jaz Murian stations. The black line represents the median estimates of apparent velocities for the real data. The gray dotted lines represent the apparent velocity curves coming from two hundred models that are closest to the real data (black line) among all models. The red line represents the best fit apparent velocity curve, while the red circle marks the best cutoff period for each inversion. (b) Inverted results from the corresponding apparent velocity curves shown in (a). The red line displays the best fit model. The thick gray lines outline the parameter space covered in the grid search, while the thin gray lines display the two hundred models which correspond to the above apparent velocity curves.

4. Discussion

The Jaz Murian Basin is a topographic-low depression with a mean elevation of ~360 m surrounded by high rocky and arid mountainous ranges more than 2000 m high. The Bampour and Halil rivers flow into the Jaz Murian Basin. During the spring season, when the rivers overflow, part of the basin is flooded and very shallow (20–30 cm) saline lakes can form, which may shrink and remain dry in summer (Atashan et al., 2017; Rashki et al., 2017; Shirani et al., 2020). The region experienced a humid climate characterized by several monsoon rain periods during the past few million years (Ivory & Lezine, 2009), possibly producing lake deposition in the Jaz Murian depression. The recent quaternary sedimentary deposits (Mccall, 2002), are probably interbedded with lavas from the nearby Taftan and Bazman volcanoes (Pang et al., 2014), and detritus from the Urumieh-Dokhtar Magmatic Arc (Ali et al., 2017), or even from the nascent Himalaya (Carter et al., 2010; Mazhar et al., 2001). This is consistent with the presence of alluvial fans of gravels, silt plains, playa lakes, dunes and salt pans in the basin and with the nature of surface rocks, mainly composed of tuffs, tuffaceous sandstones, silts and gypsums (Burg, 2018; Harrison, 1943; Mccall & Kidd, 1982). Laboratory measurements of the P-wave velocity for such sedimentary rocks range between 1.5 and 4.5 km/s (Kearey et al., 2009). Our estimates are well within the range of those laboratory measurements. In the Great Valley forearc basin located on the west coast of the United States, which is well constrained by multiple active source profiles (Colburn & Mooney, 1986; Fliedner et al., 1996; Godfrey et al., 1997; Holbrook & Mooney, 1987; Zoback & Wentworth, 1990), the P-wave velocity in the sedimentary layer is about 1.5–4 km/s. The P velocity variability results from a wide variety of deposits, from Upper Cretaceous rocks to Pliocene and Quaternary sediments (Thompson & Talwani, 1964) but they are also comparable to those measured in the Jaz Murian.

The low Versus and high Vp/Vs ratios (greater than 2.2) for the sedimentary infill may reveal unconsolidated porous sediments (e.g., Horozal et al., 2013; Wiersberg et al., 2015), or fluid saturated sediments with pore fluid connected pathways (i.e., dipping strata, fractures, and faults) that maintain the hydro-static pore pressure (Chhun & Tsuji, 2021; Donna et al., 2005; Wiersberg et al., 2015). Since the amplitudes of reflected P and S waves are

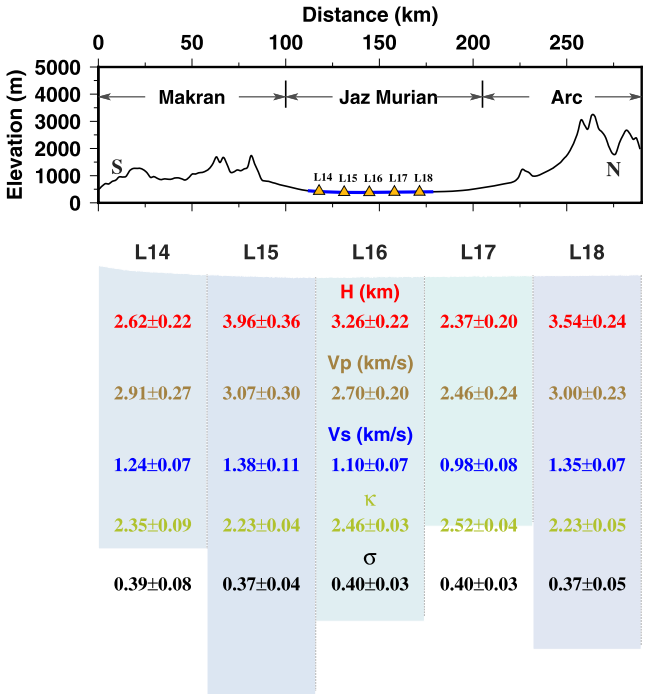

Figure 13. Structural information extracted from western Jaz Murian stations. The upper panel shows the elevation of the transect crossing the Jaz Murian Basin, whereas the lower panel shows the sedimentary layer structure beneath the five stations in western Jaz Murian Basin, including the sediment thickness (H), P wave velocity (V_P), S wave velocity (V_S), V_P/V_S ratio (κ), and Poisson's ratio (σ).

very large, this implies very low seismic velocities at the base of the sedimentary layer. This suggests that if these very low seismic velocities are related to fluid-filled porosity, this porosity is still important at depth.

In addition, our results may imply that the sedimentation in the western Jaz Murian Basin is fast, which may due to the abundant sediment sources around. Indeed, a high sedimentation rate will result in unconsolidated and high porosity deposits, which tends to reduce V_P, but even more V_S, and thus leads to increased V_P/V_S ratios (Goes & Lee, 2002; Sheriff & Geldart, 1995). In contrast, a low sedimentation rate is conducive to a more effective porosity closure, with higher V_S and lower V_P/V_S ratios.

5. Conclusions

We have exploited the autocorrelations and polarizations of teleseismic P and S waves recorded by the China-Iran geological and geophysical survey in the Iranian plateau to image the western Jaz Murian Basin (southeast Iran). The autocorrelograms revealed very strong reflection pulses from the top basement. The two-way travel times of reflected S waves and P polarization measurements allowed us to estimate an average sediment thickness of about 3 km. The very low seismic velocities (Vp ~ 2.9 km/s and Vs. ~ 1.2 km/s), and high Vp/Vs ratio (~2.4) suggest unconsolidated sediments, and thus a recent and fast deposition of the western Jar Murian Basin.

Data Availability Statement

The World Data Center (WDC) was used for access to waveform data (available from https://doi.org/10.12197/2021GA026).

Acknowledgments

This research is supported by the Strategic Priority Research Program (XDA20070302), the National Natural Science Foundation of China (42022028, 91855207, 41888101), the Open Fund Project State Key Laboratory of Lithospheric Evolution (SKL-YT201802), and also the China Scholarship Council. We appreciate the Associate Editor, and Abdolreza Ghods and one anonymous reviewer for their constructive comments and suggestions, which significantly improved the manuscript. We are thankful to Dr. Brigitte Knapmeyer-Endrun for providing the fast RF calculation package. We acknowledge Prof. Bo Holm Jacobsen for constructive comments given on Vs-apparent method. We also acknowledge Drs. Jiangang Wang, Bo Wan and Yang Chu for fruitful discussions. We appreciate the assistance of all other members of "China-Iran Geological and Geophysical Survey in the Iranian Plateau (CIGSIP)" project, who participated the collection of the data used in this study. This is a contribution to IGCP 662, IGCP 669 and IGCP 710. The receiver function and seismogram data used in the computation of the autocorrelation can be downloaded at https://doi.org/10.12197/2021GA026.

References

Abedi, M., & Bahroudi, A. (2016). A geophysical potential field study to image the Makran subduction zone in SE of Iran. *Tectonophysics*, *688*, 119–134. https://doi.org/10.1016/j.tecto.2016.09.025

Ali, A., Burg, J. P., Guillong, M., & Von Quadt, A. (2017). Arc magmatism witnessed by detrital zircon U-Pb geochronology, Hf isotopes and provenance analysis of Late Cretaceous-Miocene sandstones of onshore Western Makran (SE Iran). *American Journal of Science*, *317*(8), 941–964. https://doi.org/10.2475/08.2017.03

Amini, S., Shomali, Z. H., Koyi, H., & Roberts, R. G. (2012). Tomographic upper-mantle velocity structure beneath the Iranian Plateau. *Tectonophysics*, *554*, 42–49. https://doi.org/10.1016/j.tecto.2012.06.009

Atashan, A. K., Pourkermani, M., Bafti, A. S., Ghorashi, M., & Bouzari, S. (2017). Assessment of beshagard mountain tectonic activity (south of jazmurian depration) application IRAT index. *Open Journal of Geology*, *07*(3), 295–319. https://doi.org/10.4236/ojg.2017.73021

Backus, & George, E. (1965). Possible forms of seismic anisotropy of the uppermost mantle under oceans. *Journal of Geophysical Research*, *70*(14), 3429–3439. https://doi.org/10.1029/jz070i014p03429

Badal, J., Chen, Y., Chourak, M., & Stankiewicz, J. (2013). S-wave velocity images of the Dead Sea Basin provided by ambient seismic noise. *Journal of Asian Earth Sciences*, *75*(oct.5), 26–35. https://doi.org/10.1016/j.jseaes.2013.06.017

Bataille, K., & Chiu, J. (1991). Polarization analysis of high-frequency, three-component seismic data. *Bulletin of the Seismological Society of America*, *81*(2), 622–642. https://doi.org/10.1785/bssa0810020622

Boness, N. L., & Zoback, M. (2006). Mapping stress and structurally controlled crustal shear velocity anisotropy in California. *Geology*, *34*(10), 825–828. https://doi.org/10.1130/g22309.1

Burg, J.-P. (2018). Geology of the onshore Makran accretionary wedge: Synthesis and tectonic interpretation. *Earth-Science Reviews*, *185*, 1210–1231. https://doi.org/10.1016/j.earscirev.2018.09.011

Carter, A., Najman, Y., Bahroudi, A., Bown, P., Garzanti, E., & Lawrence, R. D. (2010). Locating earliest records of orogenesis in Western Himalaya: Evidence from Paleogene sediments in the Iranian Makran region and Pakistan Katawaz basin. *Geology*, *38*(9), 807–810. https://doi.org/10.1130/g31087.1

Chapman, C. H. (1978). A new method for computing synthetic seismograms. *Geophysical Journal International*, *54*(3), 481–518. https://doi.org/10.1111/j.1365-246X.1978.tb05491.x

Chen, L., Wen, L., & Zheng, T. (2005). A wave Equation Migration method for receiver function imaging. *Journal of Geophysical Research*, *110*(B11). https://doi.org/10.1029/2005JB003665

Chhun, C., & Tsuji, T. (2021). Pore pressure and gas saturation distribution in the forearc basin of the Nankai subduction zone inferred from high-resolution Vp and vs. *Journal of Petroleum Science and Engineering*, *205*(2), 108911. https://doi.org/10.1016/j.petrol.2021.108911

Chimoto, K., & Yamanaka, H. (2020). Tuning S-wave velocity structure of deep sedimentary layers in the Shimousa region of the Kanto basin, Japan, using autocorrelation of strong-motion records. *Bulletin of the Seismological Society of America*, *110*(6), 2882–2891. https://doi.org/10.1785/0120200156

Chong, J., Chu, R., Ni, S., Meng, Q., & Guo, A. (2018). Receiver function HV ratio, a new measurement for reducing non-uniqueness of receiver function waveform inversion. *Geophysical Journal International*(2), 1475–1485. https://doi.org/10.1093/gji/ggx464

Claerbout, J. F. (1968). Synthesis of a layered medium from its acoustic transmission response. *Geophysics*, *33*(2), 264–269. https://doi.org/10.1190/1.1439927

Colburn, R. H., & Mooney, W. D. (1986). Two-dimensional velocity structure along the synclinal axis of the Great Valley, California. *Bulletin of the Seismological Society of America*, *76*(5), 1305–1322.

Crampin, S., & Chastin, S. (2003). A review of shear wave splitting in the crack-critical crust. *Geophysical Journal International*, *155*(1), 221–240. https://doi.org/10.1046/j.1365-246X.2003.02037.x

Daley, T. M., & Mcevilly, T. V. (1990). Shear wave anisotropy in the Parkfield varian well VSP. *Bulletin of the Seismological Society of America*, *80*(4), 857–869. https://doi.org/10.1785/BSSA0800040857

Donna, E. P., Reyners, M., Chadwick, M., & Chiu, J. M. (2005). Crustal heterogeneity and subduction processes: 3-D Vp, Vp/Vs and Q in the southern north Island, New Zealand. *Geophysical Journal International*, *162*(1), 270–288. https://doi.org/10.1111/j.1365-246X.2005.02530.x

Du, Z., Foulger, G., & Mao, W. (2000). Noise reduction for broad-band, three-component seismograms using data-adaptive polarization filters. *Geophysical Journal International*, *141*(3), 820–828. https://doi.org/10.1046/j.1365-246x.2000.00156.x

Efron, B., & Tibshirani, R. (1991). Statistical data analysis in the computer age. *Science*, *253*(5018), 390–395. https://doi.org/10.1126/science.253.5018.390

Esmaeili, R., Xiao, W., Griffin, W. L., Moghadam, H. S., Zhang, Z., Ebrahimi, M., et al. (2020). Reconstructing the source and growth of the Makran accretionary complex: Constraints from detrital zircon U-Pb geochronology. *Tectonics*, *39*(2). https://doi.org/10.1029/2019TC005963

Fang, H., & Hilst, R. D. (2019). Earthquake depth phase extraction with P wave autocorrelation provides insight into Mechanisms of intermediate-depth earthquakes. *Geophysical Research Letters*, *46*(24), 14440–14449. https://doi.org/10.1029/2019GL085062

Fliedner, M. M., Ruppert, S., & Sierra, S. (1996). Nevada Continental Dynamics Working GroupThree-dimensional crustal structure of the southern Sierra Nevada from seismic fan profiles and gravity modeling. *Geology*, *24*(4), 367–370. https://doi.org/10.1130/0091-7613(1996)024<0367:tdcsot>2.3.co;2

Frasier, C. W. (1970). Discrete time solution of plane P-SV waves in a plane layered medium. *Geophysics*, *35*(2), 197–219. https://doi.org/10.1190/1.1440085

Fretwell, P., Pritchard, H. D., Vaughan, D. G., Bamber, J. L., Barrand, N. E., Bell, R., & Bianchi, C. (2013). Bedmap2: Improved ice bed, surface and thickness datasets for Antarctica. The *Cryosphere*, *7*(1), 375–393. https://doi.org/10.5194/tc-7-375-2013

Friederich, W. (1998). Wave-theoretical inversion of teleseismic surface waves in a regional network: Phase-velocity maps and a three-dimensional upper-mantle shear-wave-velocity model for southern Germany. *Geophysical Journal International*, *132*(1), 203–225. https://doi.org/10.1046/j.1365-246x.1998.00425.x

Godfrey, N., Beaudoin, B., & Klemperer, S. (1997). Ophiolitic basement to the Great Valley forearc basin, California, from seismic and gravity data: Implications for crustal growth at the North American continental margin. The *Geological Society of America Bulletin*, *109*(12), 1536–1562. https://doi.org/10.1130/0016-7606(1997)109<1536:obttgv>2.3.co;2

Goes, S., & Lee, S. (2002). Thermal structure of the North American uppermost mantle inferred from seismic tomography. *Journal of Geophysical Research*, *107*(B3). ETG2-1–ETG2-13. https://doi.org/10.1029/2000JB000049

Gorbatov, A., Saygin, E., & Kennett, B. (2013). Crustal properties from seismic station autocorrelograms. *Geophysical Journal International*, *192*(2), 861–870. https://doi.org/10.1093/gji/ggs064

Greenberg, M., & Castagna, J. (1992). Shear-wave velocity estimation in porous rocks: Theoretical formulation, preliminary verification and applications. *Geophysical Prospecting*, *40*(2), 195–209. https://doi.org/10.1111/j.1365-2478.1992.tb00371.x

Haberland, C., Mokhtari, M., Babaei, H. A., Ryberg, T., Masoodi, M., Partabian, A., & Lauterjung, J. (2021). Anatomy of a crustal-scale accretionary complex: Insights from deep seismic sounding of the onshore Western Makran subduction zone, Iran. *Geology*, *49*(1), 3–7. https://doi.org/10.1130/G47700.1

Hannemann, K., Krüger, F., Dahm, T., & Lange, D. (2016). Oceanic lithospheric S-wave velocities from the analysis of P-wave polarization at the ocean floor. *Supplements to the Monthly Notices of the Royal Astronomical Society*, *207*(3), 1796–1817. https://doi.org/10.1093/gji/ggw342

Harrison, J. (1943). The Jaz Murian depression, Persian baluchistan. *The Geographical Journal*, *101*(5/6), 206–225. https://doi.org/10.2307/1789627

Herrmann, R. B. (2013). Computer programs in seismology: An evolving tool for instruction and research. *Seismological Research Letters*, *84*(6), 1081–1088. https://doi.org/10.1785/0220110096

Holbrook, W. S., & Mooney, W. D. (1987). The crustal structure of the axis of the Great Valley, California, from seismic refraction measurements. *Tectonophysics*, *140*(1), 49–63. https://doi.org/10.1016/0040-1951(87)90139-9

Hopson, C. A., Mattinson, J. M., Pessagno, E. A., & Luyendyk, B. P. (2008). *California Coast Range Ophiolite: Composite Middle and Late Jurassic Oceanic Lithosphere* (Vol. 438, p. 1). Special Papers-Geological Society of America. https://doi.org/10.1130/2008.2438(01)

Horozal, S., Cukur, D., & Kim, G. Y. (2013). *Predicting sediment physical properties from seismic multi-attributes in the kumano forearc basin, nankai trough* (EGU2013–2661). EGU General Assembly Conference Abstracts.

Ingersoll, R. (1988). Tectonics of sedimentary basins. *Geological Society of America Bulletin*, *100*(11), 1704–1719. https://doi.org/10.1130/0016-7606(1988)100<1704:tosb>2.3.co;2

Ivory, S. J., & Lezine, A. M. (2009). Climate and environmental change at the end of the Holocene humid period: A pollen record off Pakistan. *Comptes Rendus Geoscience*, *341*(8–9), 760–769. https://doi.org/10.1016/j.crte.2008.12.009

Jiang, M., Ai, Y., Chen, L., & Yang, Y. (2013). *Local modification of the lithosphere beneath the central and Western north China Craton: 3-D constraints from Rayleigh wave tomography*, *24*(3–4), 849–864. https://doi.org/10.1016/j.gr.2012.06.018

Kearey, P., Brooks, M., & Hill, I. (2009). *An introduction to geophysical exploration*.

Kennett, B. (2015). Lithosphere-asthenosphere P-wave reflectivity across Australia. *Earth and Planetary Science Letters*, *431*, 225–235. https://doi.org/10.1016/j.epsl.2015.09.039

Kennett, B., Engdahl, E., & Buland, R. (1995). Constraints on seismic velocities in the Earth from traveltimes. *Geophysical Journal International*, *122*, 108–124. https://doi.org/10.1111/j.1365-246x.1995.tb03540.x

Lei, J., & Zhao, D. J. G. (2009). Structural heterogeneity of the Longmenshan fault zone and the mechanism of the 2008 Wenchuan earthquake (Ms 8.0). *Geophysics, Geochemistry, Geosystems*, *10*(10). https://doi.org/10.1029/2009GC002590

Liang, C., Song, X., & Huang, J. (2004). Tomographic inversion of Pn travel times in China. *Journal of Geophysical Research*, *109*. B11304. https://doi.org/10.1029/2003JB002789

Ligorria, J. P., & Ammon, C. J. (1999). Iterative deconvolution and receiver-function estimation. *Bulletin of the Seismological Society of America*, *89*(5), 1395–1400. https://doi.org/10.1785/bssa0890051395

Lin, F. C., Li, D., Clayton, R. W., & Hollis, D. (2013). High-resolution 3D shallow crustal structure in Long Beach, California: Application of ambient noise tomography on a dense seismic array. *Geophysics*, *78*(4), Q45–Q56. https://doi.org/10.1190/geo2012-0453.1

Lin, F. C., and V. C. Tsai, (2013). Seismic interferometry with antipodal station pairs, *Geophysical Research Letters*, *40*(17), 4609–4613, https://doi.org/10.1002/grl.50907

Mazhar, Q., Niem, A. R., & Lawrence, R. D. (2001). Detrital modes and provenance of the Paleogene Khojak formation in Pakistan: Implications for early Himalayan orogeny and unroofing. *GSA Bulletin*.

Mccall, G. (2002). A summary of the geology of the Iranian Makran. *Geological Society London Special Publications*, *195*(1), 147–204. https://doi.org/10.1144/gsl.sp.2002.195.01.10

Mccall, G., & Kidd, R. (1982). The Makran, southeastern Iran: The anatomy of a convergent plate margin active from Cretaceous to present. *Geological Society London Special Publications*, *10*(1), 387–397. https://doi.org/10.1144/gsl.sp.1982.010.01.26

Mooney, W. D., Laske, G., & Masters, T. G. (1998). Crust 5.1: A global crustal model at 5× 5. *Journal of Geophysical Research*, *103*(B1), 727–747. https://doi.org/10.1029/97jb02122

Nakata, N., Chang, J. P., Lawrence, J. F., & Boué, P. (2015). Body wave extraction and tomography at Long Beach, California, with ambient-noise interferometry. *Journal of Geophysical Research: Solid Earth*, *120*(2), 1159–1173. https://doi.org/10.1002/2015jb011870

Pang, K. N., Chung, S. L., Zarrinkoub, M. H., Chiu, H. Y., & Li, X. H. (2014). On the magmatic record of the Makran arc, southeastern Iran: Insights from zircon U-Pb geochronology and bulk-rock geochemistry. *Geochemistry, Geophysics, Geosystems*, *15*(6), 2151–2169. https://doi.org/10.1002/2014gc005262

Park, J., Vernon, F. L., III, & Lindberg, C. R. (1987). Frequency dependent polarization analysis of high-frequency seismograms. *Journal of Geophysical Research*, *92*(B12), 12664–12674. https://doi.org/10.1029/jb092ib12p12664

Park, S., & Ishii, M. (2018). Near-surface compressional and shear wave speeds constrained by body-wave polarization analysis. *Geophysical Journal International*, *213*(3), 1559–1571. https://doi.org/10.1093/gji/ggy072

Phạm, T.-S., & Tkalčić, H. (2017). On the feasibility and use of teleseismic P wave coda autocorrelation for mapping shallow seismic discontinuities. *Journal of Geophysical Research: Solid Earth*, *122*, 3776–3791. https://doi.org/10.1002/2017JB013975

Phạm, T. S., & Tkalčić, H. (2018). Antarctic ice properties revealed from teleseismic P wave coda autocorrelation. *Journal of Geophysical Research: Solid Earth*, *123*(9), 7896–7912. https://doi.org/10.1029/2018JB016115

Plescia, S. M., Sheehan, A. F., Haines, S. S., Worthington, L. L., Cook, S., & Ball, J. S. (2021). Teleseismic P -Wave Coda Autocorrelation Imaging of Crustal and Basin Structure, Bighorn Mountains Region, Wyoming, U.S.A. *Bulletin of the Seismological Society of America*, *111*(1), 466–475. https://doi.org/10.1785/0120200177

Priestley, K., Sobouti, F., Mokhtarzadeh, R., A Irandoust, M., Ghods, R., Motaghi, K., & Ho, T. (2022). New constraints for the on-shore Makran Subduction Zone crustal structure. *Journal of Geophysical Research: Solid Earth*, *127*, e2021JB022942. https://doi.org/10.1029/2021jb022942

Rashki, A., Arjmand, M., & Kaskaoutis, D. G. (2017). Assessment of dust activity and dust-plume pathways over Jazmurian Basin, southeast Iran. *Aeolian Research*, *24*, 145–160. https://doi.org/10.1016/j.aeolia.2017.01.002

Ritzwoller, M. H., Barmin, M. P., Villasenor, A., Levshin, A. L., & Engdahl, E. R. (2002). Pn and Sn tomography across Eurasia to improve regional seismic event locations. *Tectonophysics*, *358*(1–4), 39–55. https://doi.org/10.1016/S0040-1951(02)00416-X

Ruigrok, E., & Wapenaar, K. (2012). Global-phase seismic interferometry unveils P-wave reflectivity below the Himalayas and Tibet. *Geophysical Research Letters*, *39*(11), 11303. https://doi.org/10.1029/2012gl051672

Schimmel, M., & Paulssen, H. (1997). Noise reduction and detection of weak, coherent signals through phase-weighted stacks. *Geophysical Journal International*, *130*(2), 497–505. https://doi.org/10.1111/j.1365-246x.1997.tb05664.x

Sheriff, R. E., & Geldart, L. P. (1995). *Exploration Seismology*. Cambridge University Press. (7), 191–238. https://doi.org/10.1017/CBO9781139168359

Shirani, M., Afzali, K. N., Jahan, S., Strezov, V., & Soleimani-Sardo, M. (2020). Pollution and contamination assessment of heavy metals in the sediments of Jazmurian playa in southeast Iran. *Scientific Reports*, *10*(1), 4775. https://doi.org/10.1038/s41598-020-61838-x

Simmons, N. A., Myers, S. C., & Johannesson, G. (2011). Global-scale P wave tomography optimized for prediction of teleseismic and regional travel times for Middle East events: 2. Tomographic inversion. *Journal of Geophysical Research*, *116*(B4), B04305. https://doi.org/10.1029/2010jb007969

Smith, G., McNeill, L., Henstock, T. J., & Bull, J. (2012). The structure and fault activity of the Makran accretionary prism. *Journal of Geophysical Research*, *117*(B7). https://doi.org/10.1029/2012JB009312

Stern, R. J., Moghadam, H. S., Pirouz, M., & Mooney, W. (2021). The Geodynamic Evolution of Iran. *Annual Review of Earth and Planetary Sciences*, *49*, 9–36. https://doi.org/10.1146/annurev-earth-071620-052109

Sun, W., Fu, L., Wei, W., & Tang, Q. (2018). A new seismic daylight imaging method for determining the structure of lithospheric discontinuity. *Science China Earth Sciences*, *62*(2), 1–16. https://doi.org/10.1007/s11430-018-9249-3

Sun, W., & Kennett, B. (2016). Receiver structure from teleseisms: Autocorrelation and cross correlation. *Geophysical Research Letters*, *43*(12), 6234–6242. https://doi.org/10.1002/2016GL069564

Svenningsen, L., & Jacobsen, B. (2007). Absolute S-velocity estimation from receiver functions. *Geophysical Journal International*, *170*(3), 1089–1094. https://doi.org/10.1111/j.1365-246x.2006.03505.x

Tang, X.-M., Cheng, C. H. A., & Cheng, A. (2004). *Quantitative borehole acoustic methods*. Elsevier.

Taylor, G., Rost, S., & Houseman, G. (2016). Crustal imaging across the North Anatolian Fault Zone from the autocorrelation of ambient seismic noise. *Geophysical Research Letters*, *43*(6), 2502–2509. https://doi.org/10.1002/2016gl067715

Teknik, V., & Ghods, A. (2017). Depth of Magnetic Basement in Iran Based on Fractal Spectral Analysis. *Geophysical Journal International*, *209*(3), 1878–1891. https://doi.org/10.1093/gji/ggx132

Thompson, G. A., & Talwani, M. (1964). Crustal Structure from Pacific Basin to Central Nevada. *Journal of Geophysical Research*, *69*(22), 4813–4837. https://doi.org/10.1029/jz069i022p04813

Tian, X., Bai, Z., Klemperer, S. L., Liang, X., Liu, Z., Wang, X., et al. (2021). Crustal-scale wedge tectonics at the narrow boundary between the Tibetan Plateau and Ordos block. *Earth and Planetary Science Letters*, *554*, 116700. https://doi.org/10.1016/j.epsl.2020.116700

Tibuleac, I. M., and D. J. G. J. I. von Seggern, (2012). *Crust-mantle boundary reflectors in Nevada from ambient seismic noise autocorrelations*, *189*(1), 493–500. https://doi.org/10.1111/j.1365-246x.2011.05336.x

Vernant, P., Nilforoushan, F., Hatzfeld, D., Abbassi, M. R., Vigny, C., Masson, F., et al. (2004). Present-day crustal deformation and plate kinematics in the Middle East constrained by GPS measurements in Iran and northern Oman. *Geophysical Journal International*, *157*(1), 381–398. https://doi.org/10.1111/j.1365-246x.2004.02222.x

Vidale, J. E. (1986). Complex polarization analysis of particle motion. *Bulletin of the Seismological Society of America*, *76*(5), 1393–1405.

Wagner, G. S., & Owens, T. J. (1995). Broadband eigen-analysis for three-component seismic array data. *IEEE Transactions on Signal Processing*, *43*(7), 1738–1741. https://doi.org/10.1109/78.398741

Wang, J.-G., Hu, X., Garzanti, E., An, W., & Liu, X. C. (2017). The birth of the Xigaze forearc basin in southern Tibet. *Earth and Planetary Science Letters*, *465*, 38–47. https://doi.org/10.1016/j.epsl.2017.02.036

Wang, X., Chen, L., Ling, Y., Gao, Y., Zhang, J., & Yao, H. (2019). A new method to constrain shallow crustal S-wave velocities based on direct P-wave amplitudes in receiver functions and its application in northeastern Tibet. *Science China(Earth Sciences)*, *62*(11), 159–171. https://doi.org/10.1007/s11430-018-9443-6

Wapenaar, K., J., Thorbecke, and Draganov, D. (2004). *Relations between reflection and transmission responses of three-dimensional inhomogeneous media*, *156*(2), 179–194. https://doi.org/10.1111/j.1365-246x.2003.02152.x

Wiechert, E. (1907). U¨ber Erdbebenwellen. Part I: Theoretisches u¨ber die Ausbreitung der Erdbebenwellen, Nachrichten von der K. Gesellschaft der Wissenschaften zu Go¨ttingen. *Math. Phys. Klasse*, 415–529.

Wiersberg, T., Schleicher, A. M., Horiguchi, K., Doan, M. L., Eguchi, N., & Erzinger, J. (2015). Origin and in situ concentrations of hydrocarbons in the Kumano forearc basin from drilling mud gas monitoring during IODP NanTroSEIZE Exp. 319. *Applied Geochemistry*, *61*, 206–216. https://doi.org/10.1016/j.apgeochem.2015.06.002

Wittlinger, G., & Farra, V. (2015). Evidence of unfrozen liquids and seismic anisotropy at the base of the polar ice sheets. *Polar Science*, *9*(1), 66–79. https://doi.org/10.1016/j.polar.2014.07.006

Yilmaz, Ö. (2001). *Seismic data analysis: Processing, inversion, and interpretation of seismic data*. Society of exploration geophysicists.

Zhang, Z., Klemperer, S., Bai, Z., Chen, Y., & Teng, J. (2011). Crustal structure of the Paleozoic Kunlun orogeny from an active-source seismic profile between Moba and Guide in East Tibet. *China*, *19*(4), 994–1007. https://doi.org/10.1016/j.gr.2010.09.008

Zhu, L. (2000). Crustal structure across the San Andreas Fault, southern California from teleseismic converted waves. *Earth and Planetary Science Letters*, *179*(1), 183–190. https://doi.org/10.1016/s0012-821x(00)00101-1

Zoback, M., & Wentworth, C. (1990). *Structure of the Coalinga area and thrust origin of the earthquake* (p. 1487). United States Geological Survey, Professional Paper.